

Rate-induced tipping in a three-box AMOC model: basin dynamics and tipping probabilities

Jicheng Duan^{a, 1}

^a*School of Mathematics and Physics, China University of Geosciences, Wuhan, China*

Abstract

Rate-induced tipping in the Atlantic Meridional Overturning Circulation (AMOC) is analyzed using a three-box model.

- **Model setup:** In the frozen case the system exhibits multistability, with up to four coexisting stable equilibria.
- **Parameter drift:** The freshwater forcing F decreases linearly from $F_{\text{start}} = 0.13$ to $F_{\text{end}} = 0.10$ over a drift time T_r , giving rise to a non-autonomous system.
- **Numerical findings:**
 1. Non-autonomous basins of attraction differ from the frozen ones; both basin boundaries and relative sizes depend on the rate of change.
 2. Some trajectories switch attractors during the drift, showing partial tipping.
 3. The relative basin sizes vary with T_r , revealing critical rates: under slow drift some attractors are not reached, while under fast drift more trajectories change destination.
 4. Tipping probabilities vary continuously with T_r , indicating different sensitivities of initial conditions to the drift rate.
- **Implication:** The stability of the AMOC depends not only on the magnitude of freshwater forcing but also on its rate of change. The interplay between drift rate and the intrinsic adjustment timescale determines whether trajectories remain with the original attractor or shift to another state.

¹corresponding author. E-mail address: jichengduan9708@163.com

1. Three-box model

Let me first briefly review the structure of the model used in this paper, as well as some key results and numerical implementations from the bifurcation analysis presented in Section 3 of the study by Neff et al., titled “Bifurcation analysis of a North Atlantic Ocean box model with two deep-water formation sites”, published in *Physica D* (2023) 456: 133907.

1.1. Model 1

To investigate the stability and transitions of the Atlantic Meridional Overturning Circulation (AMOC), the authors construct a low-dimensional dynamical system consisting of three connected ocean boxes. These represent the Labrador Sea (box L), the Nordic Seas (box N), and the midlatitude Atlantic (box A). While surface temperatures T_L , T_N , and T_A are assumed to be fixed, salinities S_L , S_N , and S_A evolve dynamically and play a central role in determining water density and hence the circulation strength.

The governing equations for the salinities in the polar boxes L and N are derived from salt conservation and take the form:

$$\begin{aligned} V_L \frac{dS_L}{dt} &= -(F + F_L) S_0 + |q_L| (S_A - S_L), \\ V_N \frac{dS_N}{dt} &= -(F + F_N) S_0 + |q_N| (S_A - S_N), \end{aligned} \quad (1)$$

where F is the external freshwater forcing applied uniformly, while F_L and F_N represent background freshwater fluxes into boxes L and N , respectively. S_0 denotes a reference salinity, and V_L , V_N , and V_A are the volumes of the respective boxes. The salinity in the mid-latitude box A , denoted S_A , is not dynamically evolved but computed at each time from the global salt conservation constraint:

$$V_L S_L + V_A S_A + V_N S_N = V_{\text{tot}} S_0,$$

where $V_{\text{tot}} = V_L + V_A + V_N$ is the total ocean volume. The advective flow strengths q_L and q_N are driven by the density differences between each polar box and the mid-latitude box. Assuming linear dependence of density on temperature and salinity, the flows are given by:

$$\begin{aligned} q_L &= -k [\alpha (T_L - T_A) - \beta (S_L - S_A)], \\ q_N &= -k [\alpha (T_N - T_A) - \beta (S_N - S_A)], \end{aligned}$$

where α and β are the thermal expansion and haline contraction coefficients, respectively, and k is a hydraulic constant. Positive values of q_L and q_N correspond to downwelling (i.e., deep-water formation) in the respective polar regions.

In the symmetric version of the model, referred to as Model 1, the freshwater and thermal forcings into boxes L and N are identical. That is, $F_L = F_N$ and $T_L = T_N$. Under this assumption, the model possesses symmetry under the exchange $S_L \leftrightarrow S_N$, and the bifurcation structure is correspondingly constrained. As the control parameter F is varied, the model exhibits multiple equilibria, including a strong overturning state (pattern I), a collapsed state with

no downwelling (pattern II), and two asymmetric intermediate states (patterns III and IV) in which only one of the two polar regions sustains deep convection. However, in the symmetric model, these intermediate states are dynamically inaccessible under generic parameter sweeps, as they lie on solution branches that are not connected through bifurcations encountered during typical freshwater hosing experiments.

1.2. Model 2

To reflect the asymmetric nature of real-world AMOC, the authors introduce a generalized model, Model 2, in which asymmetries in freshwater and thermal forcing between the two polar boxes are parameterized by two quantities, η and μ . The freshwater flux into box L is interpolated as:

$$F_L = F_N + \eta (F_L^{\text{nom}} - F_N),$$

where F_N is the reference value (symmetric case), and F_L^{nom} is the observed nominal value. Similarly, the temperature of box L is set by:

$$T_L = T_N + \mu (T_L^{\text{nom}} - T_N),$$

where T_N is the fixed Nordic temperature and T_L^{nom} is the observed Labrador Sea surface temperature. The complete system is thus:

$$\begin{aligned} \frac{dS_L}{dt} &= -\frac{1}{V_L} (F + F_N + \eta (F_L - F_N)) S_0 + \frac{1}{V_L} |q_L| (S_A - S_L), \\ \frac{dS_N}{dt} &= -\frac{1}{V_N} (F + F_N) S_0 + \frac{1}{V_N} |q_N| (S_A - S_N), \\ S_A &= \frac{V_{\text{tot}} S_0 - V_L S_L - V_N S_N}{V_A}, \\ q_L &= -k [\alpha (T_N + \mu (T_L - T_N) - T_A) - \beta (S_L - S_A)], \\ q_N &= -k [\alpha (T_N - T_A) - \beta (S_N - S_A)]. \end{aligned} \tag{2}$$

When $\eta = \mu = 0$, the model reduces to the symmetric configuration (Model 1). When $\eta = \mu = 1$, it reflects full observational asymmetry.

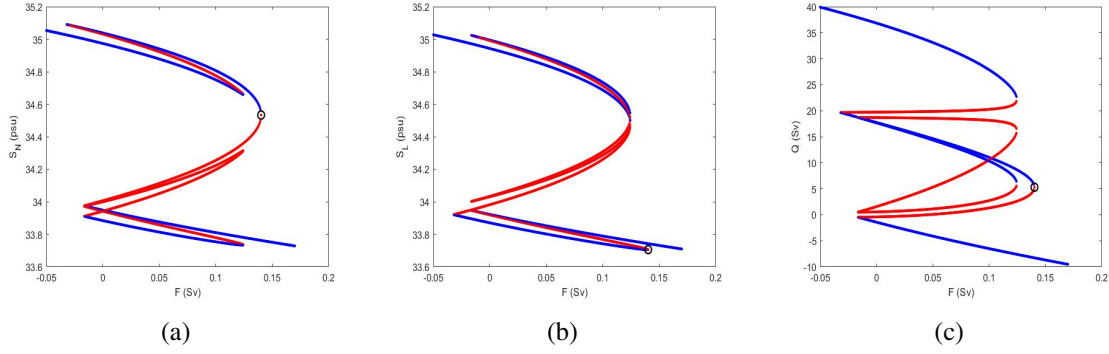


Figure 1: Bifurcation diagram for the asymmetric case $(\eta, \mu) = (1, 0)$. The control parameter is the freshwater forcing F . **Blue** curves indicate branches of stable equilibria, while **red** curves denote unstable or saddle-type equilibria.

The introduction of asymmetry breaks the degeneracy of the fold bifurcations: instead of a simultaneous collapse of multiple equilibrium branches, the model exhibits distinct bifurcation points associated with different collapse paths. Notably, pattern IV, in which only the Nordic Seas remain active, becomes a dynamically accessible intermediate state. As freshwater forcing increases, the system may follow a multi-stage tipping path, transitioning from pattern I (both L and N active), through pattern IV (only N active), to pattern II (no deep-water formation). A reverse path may be followed during recovery. Additionally, the type of asymmetry plays a distinct role in the bifurcation behavior. Freshwater asymmetry, controlled by η , primarily affects the fold bifurcations at lower values of F , shifting the location where the lower branch (pattern II) terminates. In contrast, thermal asymmetry, governed by μ , more strongly influences the upper branch. In particular, it destabilizes the strong circulation state at a lower F value and causes pattern III (only L active) to exist as an isolated branch (isola), which cannot be accessed without carefully tuned initial conditions. Figure 1 a reproduction of Fig. 7 from Sec. 3.2.

Table 1: Equilibria and fluxes corresponding to Fig. 2(a) ($Q = q_L + q_N$).

Type	SL	SN	q_L	q_N	Q
Stable equilibrium	33.74	34.81	-3.43	14.46	11.03
Saddle equilibrium	33.77	34.25	-3.43	4.74	1.31
Stable equilibrium	33.79	33.81	-3.43	-3.08	-6.51
Saddle equilibrium	34.26	34.78	5.80	14.46	20.26
Unstable equilibrium	34.29	34.22	5.80	4.74	10.54
Saddle equilibrium	34.31	33.78	5.80	-3.08	2.72
Stable equilibrium	34.69	34.75	13.40	14.46	27.87
Saddle equilibrium	34.71	34.20	13.40	4.74	18.14
Stable equilibrium	34.73	33.75	13.40	-3.08	10.33

In AMOC system, the freshwater forcing F acts as an external driver. We analyze the phase-plane dynamics in the (S_L, S_N) coordinates by means of nullclines, given by the algebraic re-

lations $\dot{S}_L = 0$ and $\dot{S}_N = 0$. For the parameter choice $\eta = 1$ and $\mu = 0$, these nullclines are approximately straight, gently sloped curves in the observed range of salinities. Their intersections are the steady states of the frozen-in system (System 2) for a fixed F . The linear stability of each equilibrium is obtained from the eigenvalues of the Jacobian evaluated at the corresponding point. At $F = 0.10$, the (S_L, S_N) phase plane exhibits a multistability with nine equilibria in total (Table 1). Among them, four are stable nodes located near $(S_L, S_N) \approx (33.74, 34.81)$, $(33.79, 33.81)$, $(34.69, 34.75)$, and $(34.73, 33.75)$. These equilibria correspond to qualitatively distinct circulation regimes, as reflected in their overturning fluxes: the northern branch q_N can be strongly positive (14.46), moderately negative (-3.08), or weakly positive depending on the attractor, while the southern branch q_L varies between -3.43 and 13.40. The unstable equilibrium, located at $(34.29, 34.22)$, together with four saddle points, organizes the basin geometry by forming the separatrices between the different basins of attraction. In fact, Fig. 2(c) shows that the state space is partitioned into four major basins of attraction, separated by invariant manifolds of the saddles. Each basin corresponds to convergence towards one of the stable equilibria, and their relative extent indicates that multiple circulation states coexist under the same external forcing. When the freshwater forcing is increased to $F = 0.13$, several equilibria vanish through saddle-node collisions, and the system retains only three steady states in the (S_L, S_N) plane (Fig. 2b). Specifically, two of them are stable nodes and one is a saddle. Compared with the case $F = 0.10$, where nine equilibria existed, the disappearance of intermediate branches leads to a simplified phase-space structure. The basin diagram in Fig. 2(d) confirms this reduction: the state space is now divided into only two stable basins separated by a single saddle. Thus, a moderate increase in freshwater forcing directly reduces the number of admissible equilibria from nine to three, with the corresponding basins reorganized accordingly.

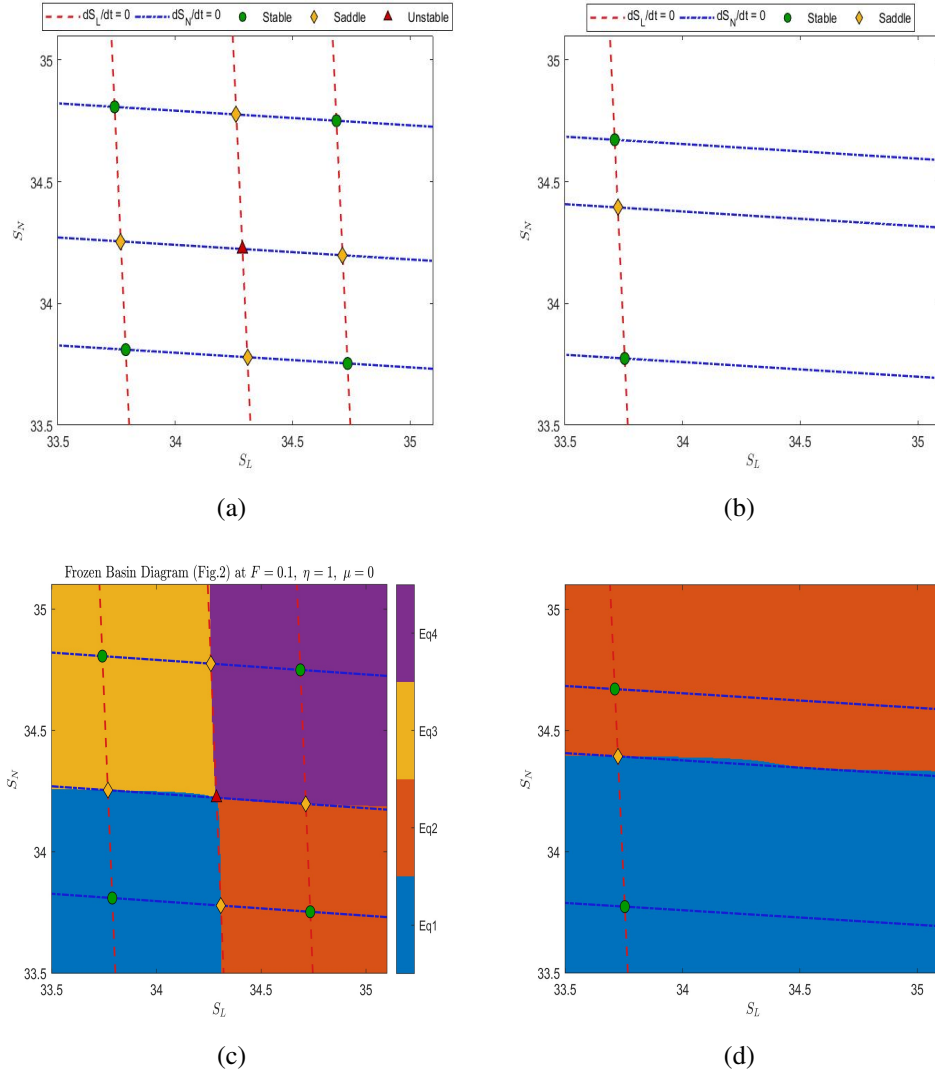


Figure 2: Nullclines and equilibria in the (S_L, S_N) phase plane with parameters $\eta = 1$ and $\mu = 0$. Red dashed lines denote $dS_L/dt = 0$, blue dash-dotted lines denote $dS_N/dt = 0$. Equilibria are classified as stable (green circles), saddle (yellow diamonds), and unstable (red triangles). Panel (a) corresponds to $F = 0.10$ (see also Table 1 for the detailed equilibrium values), showing multiple equilibria. Panel (b) corresponds to $F = 0.13$, where only three equilibria exist.

It is important to note that this system, whether in the symmetric or asymmetric configuration, exhibits multistability under certain parameter conditions. In particular, there can be up to four coexisting stable equilibria, a structural property that will be crucial for the subsequent analysis of rate-induced tipping.

2. Rate-tipping formulation of the AMOC system

In the previous section we analyzed the equilibria and multistability of the AMOC model under frozen freshwater forcing, i.e., when the control parameter F is fixed in time. However, in realistic climate scenarios external forcings such as freshwater fluxes do not remain constant, but rather evolve gradually due to processes like ice melt or changes in the hydrological cycle. To capture such transient effects, we extend the model into a non-autonomous setting by allowing F to vary in time.

Here we adopt a piecewise linear protocol for the freshwater forcing, decreasing F at a constant rate from an initial value $F_{\text{start}} = 0.13$ to a final value $F_{\text{end}} = 0.10$ during a ramping interval of length T_r , after which it is kept constant. This choice is motivated by two considerations. First, the linear drift is a widely used and analytically tractable way of representing gradual environmental change, making the results directly comparable to existing studies on rate-induced tipping. Second, the frozen-in equilibria and basins can be computed separately at the start ($F = F_{\text{start}}$) and at the end ($F = F_{\text{end}}$). This allows us to quantify explicitly how the gradual parameter drift modifies the basin geometry and, depending on the ramping rate $1/T_r$, may induce transitions between competing equilibria.

Formally, the forcing is given by

$$F(t) = \begin{cases} F_{\text{start}} + \frac{F_{\text{end}} - F_{\text{start}}}{T_r} t, & 0 \leq t \leq T_r, \\ F_{\text{end}}, & t > T_r, \end{cases} \quad (3)$$

which turns the AMOC model into a time-dependent dynamical system:

$$\begin{aligned} \frac{dS_L}{dt} &= -\frac{1}{V_L} (F(t) + F_N + \eta (F_L - F_N)) S_0 + \frac{1}{V_L} |q_L| (S_A - S_L), \\ \frac{dS_N}{dt} &= -\frac{1}{V_N} (F(t) + F_N) S_0 + \frac{1}{V_N} |q_N| (S_A - S_N), \\ S_A &= \frac{V_{\text{tot}} S_0 - V_L S_L - V_N S_N}{V_A}, \\ q_L &= -k [\alpha (T_N + \mu (T_L - T_N) - T_A) - \beta (S_L - S_A)], \\ q_N &= -k [\alpha (T_N - T_A) - \beta (S_N - S_A)]. \end{aligned} \quad (4)$$

In this formulation the system is explicitly non-autonomous through the ramping term $F(t)$. The rate $1/T_r$ becomes an additional parameter that controls whether trajectories can track their initial attractors or instead undergo rate-induced basin crossings.

Figure 3 illustrates the non-autonomous basins of attraction for the AMOC system when the freshwater forcing is linearly decreased from $F_{\text{start}} = 0.13$ to $F_{\text{end}} = 0.10$, with two different ramping times $T_r = 9$ (panel a) and $T_r = 14$ (panel b). A grid of initial conditions has been integrated, and the outcomes are color-coded according to the final attractors. In addition, four

representative trajectories are highlighted, corresponding to the initial conditions

$$\mathbf{x}_0^{(1)} = (34.88, 33.83), \quad \mathbf{x}_0^{(2)} = (34.82, 34.44), \quad \mathbf{x}_0^{(3)} = (33.61, 34.49), \quad \mathbf{x}_0^{(4)} = (34.00, 33.50).$$

For the relatively fast drift ($T_r = 9$, Fig. 3a), the basins of attraction undergo a significant rearrangement compared to the frozen-in case. In particular, the trajectories starting from $\mathbf{x}_0^{(1)}$ and $\mathbf{x}_0^{(2)}$, which in the frozen-in setting would have converged to the strong overturning state (characterized by large Q), are diverted during the parameter drift and instead approach alternative stable equilibria. This indicates rate-induced tipping: the non-autonomous basin boundaries emerging during the drift prevent these trajectories from tracking the quasi-stationary attractors. By contrast, the trajectories initialized at $\mathbf{x}_0^{(3)}$ and $\mathbf{x}_0^{(4)}$ remain within their respective basins and converge to the weak overturning states (lower Q), consistent with the frozen-in picture. Thus, depending on the initial condition, both tipping and non-tipping behavior coexist when the rate of change is sufficiently fast.

When the ramping is slower ($T_r = 14$, Fig. 3b), the outcome is markedly different. All four representative trajectories now converge to the attractors predicted by the frozen-in case: $\mathbf{x}_0^{(1)}$ and $\mathbf{x}_0^{(2)}$ approach the strong overturning branch, while $\mathbf{x}_0^{(3)}$ and $\mathbf{x}_0^{(4)}$ relax towards weak circulation states. Because the environmental forcing changes more slowly, the system has enough time to adjust, and the trajectories remain close to the quasi-stationary attractors throughout the drift.

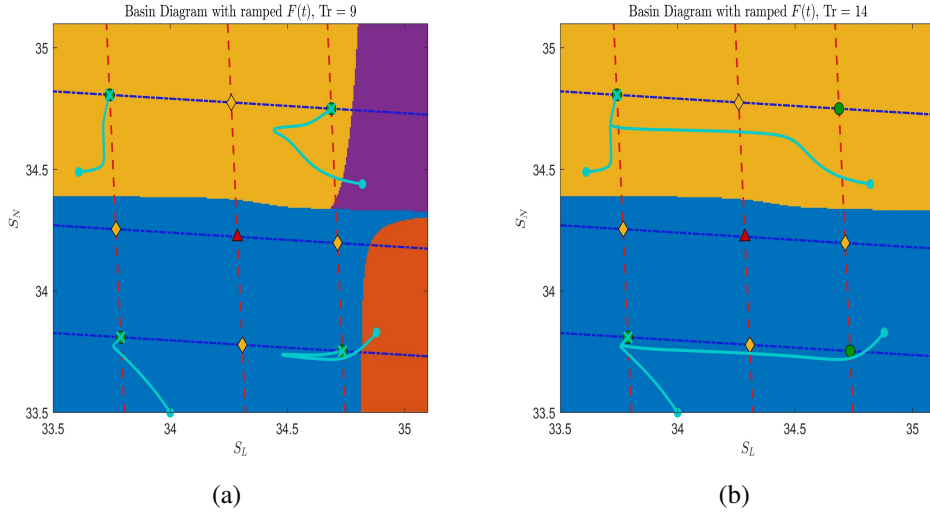


Figure 3: Time evolution of the non-autonomous AMOC system (Eq. (4)) with linearly decreasing freshwater forcing $F(t)$ from $F_{\text{start}} = 0.13$ to $F_{\text{end}} = 0.10$. Four representative trajectories are shown in cyan, starting from the initial conditions $\mathbf{x}_0^{(1)} = (34.88, 33.83)$, $\mathbf{x}_0^{(2)} = (34.82, 34.44)$, $\mathbf{x}_0^{(3)} = (33.61, 34.49)$, and $\mathbf{x}_0^{(4)} = (34.00, 33.50)$. (a) Fast drift with $T_r = 9$, (b) slow drift with $T_r = 14$. Stable equilibria are indicated by green circles, saddles by yellow diamonds, and unstable equilibria by red triangles. Red dashed lines denote the nullclines $dS_L/dt = 0$, and blue dash-dotted lines denote $dS_N/dt = 0$. The non-autonomous basins of attraction $\tilde{\mathcal{B}}$ at the end of the simulation are represented by blue, orange, purple, and reddish-orange, respectively.

Overall, comparing Fig. 3 with the frozen-in basins (Fig. 2) reveals that the non-autonomous basins of attraction $\tilde{\mathcal{B}}$ differ substantially from their frozen-in counterparts \mathcal{B} . The location of the basin boundaries, as well as the relative size of the basins, depends crucially on the rate of change of the freshwater forcing. New saddle points and their stable manifolds may emerge during the drift, but unlike in the autonomous case, these manifolds do not necessarily coincide with the boundaries of the non-autonomous basins. Indeed, as seen in panel (a), the saddle point does not lie on the actual basin boundary of $\tilde{\mathcal{B}}$, highlighting that the geometry of the non-autonomous basins cannot be inferred directly from the frozen-in picture. This distinction is essential for understanding rate-induced tipping in the AMOC: rapid forcing changes can mask or reshape bifurcations, leading to unexpected attractor switching that would not occur under frozen-in conditions.

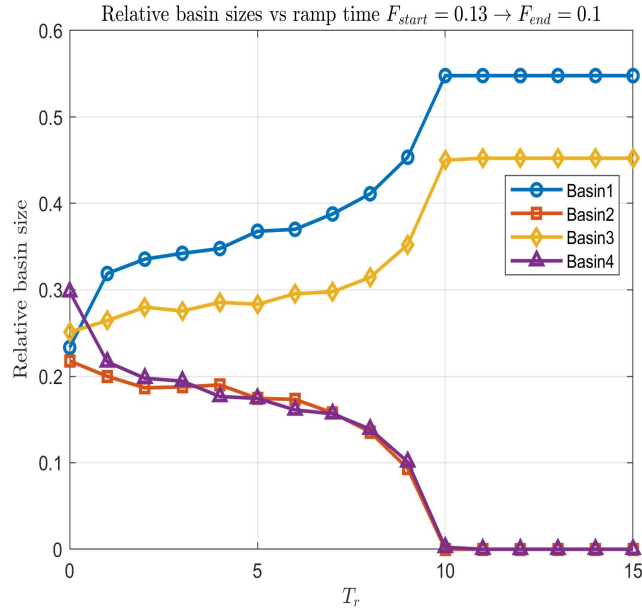


Figure 4: Relative basin sizes of the non-autonomous system with ramped freshwater forcing $F(t)$ from $F_{\text{start}} = 0.13$ to $F_{\text{end}} = 0.10$ as a function of the ramp time T_r . The relative sizes are computed at the end of the parameter drift and normalized by the total grid of initial conditions. Four curves are shown: Basin 1 (blue circles), Basin 2 (orange squares), Basin 3 (yellow diamonds), and Basin 4 (purple triangles). The figure illustrates how the relative size of each basin depends on the rate of change of $F(t)$: for small T_r the basins are of comparable size, while for large T_r the basins associated with weaker circulation (Basin 1 and Basin 3) dominate and those corresponding to stronger circulation (Basin 2 and Basin 4) vanish.

After analyzing the non-autonomous basins and representative trajectories under parameter drift, we now quantify how the rate of freshwater forcing influences the distribution of long-term outcomes. Specifically, we study how the relative sizes of the non-autonomous basins of attraction vary with the ramping time T_r . This provides a way to measure whether all possible equilibria remain relevant under time-dependent forcing, or whether some of them disappear as a consequence of the rate of change. For this purpose, we compute the relative basin size of each

non-autonomous basin $\tilde{\mathcal{B}}$ at the end of the parameter drift as a function of T_r , with the forcing decreasing linearly from $F_{\text{start}} = 0.13$ to $F_{\text{end}} = 0.10$. The results are shown in Fig. 4. For short ramping times (fast drift), four basins are present with comparable sizes. As T_r increases, the basins associated with equilibria 2 and 4 shrink and eventually vanish around $T_r \approx 10$. Beyond this value, only two stable basins remain, meaning that trajectories are funneled into fewer long-term states.

The mechanism behind this transition can be explained by a competition of timescales. When the forcing changes rapidly (small T_r), trajectories do not have enough time to approach their former attractors before new basin boundaries appear, so the newly created equilibria remain accessible. When the forcing changes slowly (large T_r), trajectories converge close to their original equilibria before the bifurcation occurs, so the new equilibria remain hidden. This explains why the non-autonomous basins $\tilde{\mathcal{B}}$ differ from the frozen-in basins \mathcal{B} and why part of the multistability structure disappears for large T_r .

To connect this with tipping probabilities, we adopt the approach of Kaszás et al. (2019). We define the probability that trajectories starting in the frozen-in basin of attractor \mathcal{A}_1 tip into another attractor $\tilde{\mathcal{A}}_2$ during the parameter drift as

$$\mathcal{P}_{\mathcal{A}_1\mathcal{A}_2} = \frac{\tilde{\mathcal{B}}(\tilde{\mathcal{A}}_2) \cap \mathcal{B}(\mathcal{A}_1)}{\mathcal{B}(\mathcal{A}_1)}.$$

In words, this is the fraction of initial conditions that would have converged to \mathcal{A}_1 in the frozen-in case, but under the parameter drift end up in $\tilde{\mathcal{A}}_2$. The continuous variation of basin sizes in Fig. 4 already suggests that such tipping probabilities will change gradually with T_r , indicating partial tipping rather than a sharp threshold.

We now complement the relative basin size analysis with a calculation of tipping probabilities between attractors, following the definition. This provides a more detailed picture of how trajectories redistribute among the possible equilibria under different ramping times T_r . The results are summarized in Fig. 5. Each panel shows the probability that initial conditions, which would converge to a given equilibrium in the frozen-in case, end up in another equilibrium after the parameter drift.

For Basin 1, the dominant outcome is self-persistence: the probability $\mathcal{P}_{\mathcal{A}_1\mathcal{A}_1}$ increases with T_r and reaches nearly one once $T_r \gtrsim 10$, consistent with the disappearance of alternative basins in Fig. 4. At small T_r , however, a non-negligible fraction of trajectories starting in Basin 1 tip into Basin 4, reflecting the influence of the fast-changing basin boundaries. For Basin 2, a similar pattern is found: $\mathcal{P}_{\mathcal{A}_2\mathcal{A}_2}$ increases with T_r , while $\mathcal{P}_{\mathcal{A}_2\mathcal{A}_3}$ decreases and eventually vanishes around $T_r \approx 10$. Transitions from Basins 1 or 2 into Basins 2 or 3 occur only at small or intermediate T_r , and their probabilities rapidly decline with increasing ramp time. In all cases, the transition probabilities vary continuously with T_r , indicating partial tipping: each trajectory has its own effective threshold depending on its initial location relative to the evolving basin boundaries.

Taken together, Figs. 4 and 5 show that the rate of freshwater forcing plays a decisive role in shaping which equilibria of the AMOC remain dynamically accessible. For fast changes

(small T_r), the system explores multiple equilibria, and tipping between basins is common. For slow changes (large T_r), some equilibria are effectively masked, and the system settles into fewer long-term outcomes. In the climate context, this suggests that the detectability of multiple AMOC states depends not only on the background freshwater forcing but also on the timescale of its variation. If external perturbations evolve slowly compared to the internal adjustment timescale of the overturning, trajectories will remain confined near the existing equilibria, and newly emerging states will not be realized. By contrast, if external perturbations evolve rapidly, the AMOC may undergo rate-induced transitions, leading to redistribution across basins and potentially abrupt shifts in circulation strength.

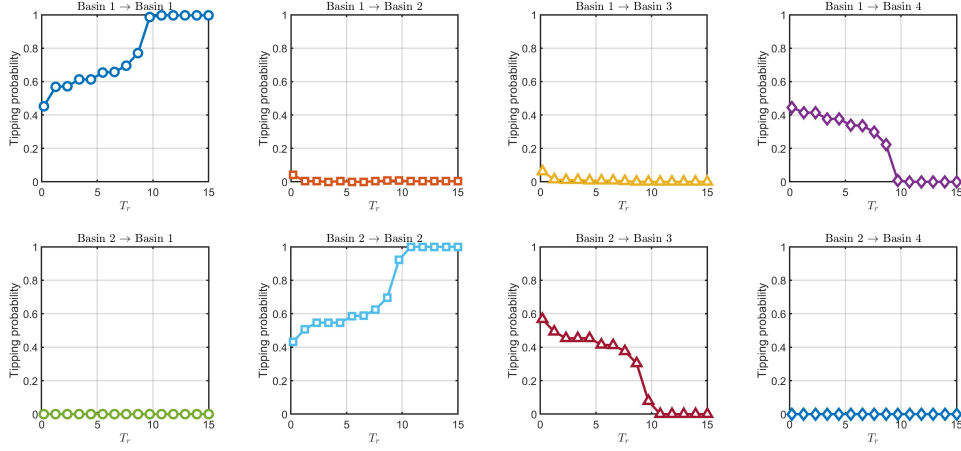


Figure 5: Tipping probabilities for the non-autonomous system with freshwater forcing ramped from $F_{\text{start}} = 0.13$ to $F_{\text{end}} = 0.10$, shown as a function of the ramp time T_r . Each panel corresponds to trajectories starting in one frozen-in basin at $t = 0$ and ending in one of the possible basins at $t = T_{\text{end}}$. The curves indicate how the chance of remaining in the original basin or moving to another basin changes with the rate of forcing, with slower ramps favoring persistence and faster ramps allowing transitions to alternative equilibria.

References

- [1] P. Ashwin, S. Wiczorek, R. Vitolo, and P. Cox. Tipping points in open systems: bifurcation, noise-induced and rate-dependent examples in the climate system. *Philosophical Transactions of the Royal Society A: Mathematical, Physical and Engineering Sciences*, **370** (2012) 1166–1184.
- [2] A. Neff, A. Keane, H. A. Dijkstra, and R. V. Donner. Bifurcation analysis of a North Atlantic Ocean box model with two deep-water formation sites. *Physica D: Nonlinear Phenomena*, **456** (2023) 133907.
- [3] P. Ashwin, C. Perryman, and S. Wiczorek. Parameter shifts for nonautonomous systems in low dimension: bifurcation- and rate-induced tipping. *Nonlinearity*, **30** (2017) 2185–2210.
- [4] B. Kaszás, U. Feudel, and T. Tél. Tipping phenomena in typical dynamical systems subjected to parameter drift. *Scientific Reports*, **9** (2019) 8654.
- [5] C. Budd and R. Kuske. Dynamic tipping and cyclic folds in a one-dimensional non-smooth dynamical system linked to climate models. *Physica D: Nonlinear Phenomena*, **457** (2024) 133949.